

# S<sup>2</sup>VG: 3D Stereoscopic and Spatial Video Generation via Denoising Frame Matrix

Peng Dai, Feitong Tan, Qiangeng Xu, Yihua Huang, David Futschik, Ruofei Du, Sean Fanello, Yinda Zhang<sup>†</sup>, Xiaojuan Qi<sup>†</sup>

**Abstract**—While video generation models excel at producing high-quality monocular videos, generating 3D stereoscopic and spatial videos for immersive applications remains an underexplored challenge. We present a pose-free and training-free method that leverages an off-the-shelf monocular video generation model to produce immersive 3D videos. Our approach first warps the generated monocular video into pre-defined camera viewpoints using estimated depth information, then applies a novel *frame matrix* inpainting framework. This framework utilizes the original video generation model to synthesize missing content across different viewpoints and timestamps, ensuring spatial and temporal consistency without requiring additional model fine-tuning. Moreover, we develop a disocclusion boundary re-injection scheme that further improves the quality of video inpainting by alleviating the negative effects propagated from disoccluded areas in the latent space. The resulting multi-view videos are then adapted into stereoscopic pairs or optimized into 4D Gaussians for spatial video synthesis. We validate the efficacy of our proposed method by conducting experiments on videos from various generative models, such as Sora, Lumiere, WALT, and Zeroscope. The experiments demonstrate that our method has a significant improvement over previous methods. Project page at: [https://daipengwa.github.io/S-2VG\\_ProjectPage/](https://daipengwa.github.io/S-2VG_ProjectPage/)

**Index Terms**—Video generation, Stereoscopic video, Spatial video, Inpainting, Diffusion model, Frame matrix, 4D Gaussian.

## 1 INTRODUCTION

THE rapid advancement of VR/AR technologies has created a growing demand for high-quality stereoscopic content capable of delivering truly immersive 3D experiences. Such content must maintain perfect 3D and semantic coherence between views while ensuring seamless temporal consistency across frames. Although monocular video generation has achieved remarkable progress, with current methods producing high-fidelity videos from complex text prompts [1], generating scene-level immersive 3D videos, encompassing both stereoscopic and spatial videos, remains an open challenge. This gap primarily arises from data limitations: while abundant training data exists for monocular video generation, comparable stereoscopic and multi-view video datasets remain scarce.

An emerging solution is to render immersive 3D videos from monocular videos using novel view synthesis [2, 3]. However, these reconstruction-based methods face two fundamental limitations. First, these reconstruction methods cannot generate plausible content for occluded regions absent from the input frames. Second, these approaches critically depend on highly accurate camera pose estimation, which is still challenging and unstable. Both structure-from-motion (SFM) [4] and joint optimization [3] easily lead to instability, particularly in dynamic scenes with subtle camera motions or when dynamic objects with temporal appearance variations dominate the visual content.

In this work, we first present a novel pose-free and training-free framework, for the sake of robustness and generalization capability, that uniquely leverages inference from an off-the-shelf video generation model [5] to produce high-quality 3D

stereoscopic videos. Our initial attempt follows a typical 2D-to-3D image uplifting methodology [6] and extends it to the video domain. Specifically, we begin by generating a monocular video as the left view, which is then warped into the right view using estimated monocular depths [7], where we apply temporal smoothing to enhance the consistency of estimated depths and meticulously develop an outpainting and multi-plane warping pipeline to mitigate artifacts, such as cracks, isolated points, and partially observed content, caused by non-watertight and narrow-FOV RGB-D frames (see Fig. 14 and Fig. 15). Subsequently, we employ an off-the-shelf video generation model [5] to synthesize natural right-view videos. This is achieved by iteratively adding and removing noise from warped frames, effectively inpainting disoccluded regions caused by the parallax of two views, drawing inspiration from diffusion-based image inpainting [8].

However, this naive approach yields suboptimal results, as independently inpainting right-view frames without referring to left-view frames introduces semantic inconsistencies across views. To address this, we propose a novel *frame matrix* representation that contains frame sequences observed from multiple virtual viewpoints uniformly distributed along the interocular axis (Fig. 2, left). The frame matrix simultaneously encodes temporal and spatial information: each row corresponds to a video sequence with continuous camera motion at a fixed timestamp (spatial direction), while each column captures dynamic scene motions across time (temporal direction), as illustrated in Fig. 1 (second column). Capitalizing on the inherent video priors of scene and camera motions within the video generation model, we propose a joint optimization strategy that updates the entire *frame matrix* along both temporal and spatial dimensions. During the denoising process, we employ resampling techniques [9] to alternately refine frame sequences along the temporal and spatial directions, progressively enhancing both temporal stability and view coherence. The final 3D stereoscopic video is constructed by selecting the

- Peng Dai, Yihua Huang, Xiaojuan Qi are with the Department of Electrical and Electronic Engineering at The University of Hong Kong, Hong Kong.
- Feitong Tan, Qiangeng Xu, David Futschik, Ruofei Du, Sean Fanello, Yinda Zhang are with Google, USA.
- <sup>†</sup> indicates corresponding author

leftmost and rightmost frame sequences as the left-eye and right-eye view videos, respectively. Since high resolution is desirable in VR applications, we also explore stereoscopic video up-sampling in our method.

Beyond stereoscopic videos with fixed viewpoints, we further develop our method to create spatial videos enabling dynamic viewpoint changes. This is achieved by initializing the frame matrix’s spatial dimension with multiple virtual viewpoints surrounding the input reference video (Fig. 2, right), followed by optimizing the inpainted frame matrix into a 4D Gaussian representation [10] to support downstream stereoscopic novel view synthesis. At each timestamp, the 3D geometry can be optimized using multi-view images with manually defined camera poses. Nevertheless, modeling continuous scene changes over time remains challenging due to the non-trivial task of estimating camera poses from a monocular video. To address this, we circumvent cross-time camera pose estimation by transferring camera motions into scene motions and modeling scene dynamics via learning time-dependent deformation offsets for each Gaussian entity. This representation naturally accommodates viewpoint changes while maintaining temporal continuity.

Furthermore, we observe that the inevitable resolution down-sampling in latent-space video generation models is detrimental to the video inpainting task. During encoding, dark disoccluded pixels propagate through the network architecture, leading to corrupted boundary features and visually apparent artifacts, as demonstrated in Fig. 12. Contrary to conventional inpainting methods [8] that perform a single encoding of masked images into latent space, our approach implements an iterative dual-space refinement and re-injection strategy. Throughout the denoising process, we simultaneously update both the disoccluded regions in image space and their corresponding latent feature representations. By re-encoding the progressively improved images, this approach purifies contaminated boundary features, leading to high-quality, artifact-free inpainting results.

To validate the efficacy of our method, we generate stereoscopic and spatial videos from monocular inputs produced by Sora [1], Lumiere [11], WALT [12], and Zeroscope [5]. Comprehensive qualitative and quantitative evaluations demonstrate that our approach consistently outperforms existing baselines in immersive 3D video generation across multiple metrics. The key contributions of our work can be summarized as follows:

- We design a novel stereoscopic and spatial video generation pipeline that eliminates the need for camera pose estimation or dataset-specific fine-tuning. To the best of our knowledge, our lines of work are pioneers in leveraging video diffusion models to facilitate the creation of immersive video.
- We propose a novel *frame matrix* representation that regularizes the diffusion-based video inpainting to generate semantically coherent and temporally consistent content.
- We meticulously develop a warping pipeline to provide correct occlusion relationships and propose a re-injection scheme that effectively mitigates the adverse effects of disoccluded regions in the latent space.
- We optimize the generated discrete observations into a continuous 4D Gaussian representation, enabling novel-time and novel-view stereoscopic video synthesis. By treating each Gaussian as a dynamic entity, we circumvent the challenging cross-time camera pose estimation.
- We conduct comprehensive experiments that show the superiority of our approach over previous methods for immersive 3D video generation.

**Difference to Our Conference Paper.** This manuscript substantially extends the ICLR 2025 conference paper [13] in the following aspects: (1) *Spatial video generation*. Unlike the conference version, which focuses on generating stereoscopic videos by taking the leftmost and rightmost columns of the denoised frame matrix, we optimize the full frame matrix, with cameras surrounding the input view, into a 4D Gaussian representation, which enables the generation of immersive spatial videos that support viewpoint changes. This optimization eliminates the need for cross-time camera pose estimation by modeling each Gaussian as a dynamic entity. (2) *Partially observed objects*. Partially observed objects in monocular videos often lead to erroneous occlusion relationships when warping to a new viewpoint, resulting in incomplete content in the final result. To address this challenge, we explore the video outpainting, which provides more complete shapes, and propose an outpainting-then-inpainting design to produce results with complete objects. (3) *Stereoscopic video super resolution*. We provide a stereoscopic video upsampling scheme that explicitly maintains the consistency between the left and right views during the video upsampling process.

## 2 RELATED WORK

**Video Generation.** Video generation has witnessed remarkable advancements since the introduction of diffusion models [14, 15]. Current state-of-the-art approaches [5, 1, 11, 12, 16, 17, 18, 19] typically address the challenge of limited annotated video data by extending pre-trained image generation models [20, 21, 22] through the insertion of temporal layers followed by video-domain fine-tuning [23, 24, 25]. Recent innovations in computational efficiency, exemplified by WALT [12] and Lumiere [11], employ joint temporal-spatial compression to enable longer video generation. The field has further progressed with Sora [1], which leverages a transformer-based diffusion architecture [26] trained on massive video datasets to achieve unprecedented generation quality. While existing work predominantly focuses on enhancing monocular video quality and duration, our research explores an orthogonal direction: harnessing these pre-trained video generation models for high-quality stereoscopic and spatial video synthesis.

**Novel View Synthesis.** Novel view synthesis has advanced significantly for both static and dynamic scenes [27, 28, 29, 30, 31, 32, 33, 34]. Early work [32] demonstrated single-image view synthesis through multi-plane representations, while [27] introduced neural radiance fields (NeRF) that revolutionized static scene rendering through volumetric representations. Subsequent approaches extended these capabilities to dynamic scenes by incorporating deformation fields [35, 36, 37] or scene flow estimation [38]. Alternative paradigms emerged with methods like DynIBaR [2], which leveraged motion fields and frame-based rendering, and RoDynRF [3] that jointly optimized scene geometry and camera poses. The field further progressed with plane-based representations as shown in FVS [39], enabling efficient novel view video synthesis. While these methods support stereoscopic view synthesis and achieve impressive results, they remain fundamentally constrained by their dependence on accurate camera pose estimation and limited ability to synthesize unseen content. Our work breaks from this paradigm by eliminating the need

for explicit pose estimation and introducing content hallucination capabilities, enabling stereoscopic and spatial video generation in challenging scenarios where traditional approaches fail.

**Content Creation and Inpainting.** Automated 3D content creation [6, 40, 41, 42, 43] represents another relevant research direction. Current approaches employ various strategies, including inpainting and multi-view generation [44, 45, 46]. In particular, some works converted RGB-D images into layered depth images for 3D photo creation [47, 48], enabling observations from different viewpoints. To enlarge the viewpoint changes, Text2Room [6] demonstrated room-scale 3D generation by progressively warping images into novel views and using text-guided inpainting for disocclusions, while WonderJourney [42] automated this process through large language model integration. Although pretrained video inpainters [49, 50] could theoretically extend these approaches to dynamic content, they struggle to produce high-quality, consistent 3D results. Deep3D [51] offers stereoscopic video conversion but requires proprietary 3D movie data and lacks flexibility for creative applications like adjustable stereo baselines. Our work explores an alternative paradigm: leveraging video generation models for immersive 3D video creation without requiring specialized training datasets.

### 3 METHOD

#### 3.1 Overview

**Stereoscopic Video Generation.** Conditioned on a text prompt or a single image  $c$ , our method aims to generate immersive 3D video  $\{\mathbf{X}_l, \mathbf{X}_r\}$ , consisting of two monocular sequences representing left and right views. The generated videos should satisfy the following three critical properties: (1) the appearance and semantics between the left  $\mathbf{X}_l$  and right  $\mathbf{X}_r$  views should be consistent and be temporally stable, (2) prominent and immersive 3D effects, and (3) diverse yet controllable output conditioned on the input.

In this work, we propose a training-free pipeline that leverages an off-the-shelf depth estimator [7] and a pretrained monocular video diffusion model  $\mathcal{G}$  (e.g., Zeroscope [5]) for 3D stereoscopic video generation. Our pipeline begins by generating a monocular video for the left view using a video diffusion model (Eq. 1,  $\epsilon_t \sim \mathcal{N}(\mathbf{0}, \mathbf{I})$  denotes the Gaussian noise sampled at diffusion timestep  $t$ ). To produce the corresponding right view while maintaining 3D consistency, we first estimate depth  $\mathbf{d}_l$  from the left view video, then apply stereoscopic warping [34, 33] to obtain the initial right view sequence  $\mathbf{X}_{l \rightarrow r}$  and its disocclusion masks  $\mathbf{M}_r$  (Eq. 2). The disoccluded regions are then completed through a diffusion-based inpainting process (Eq. 3) [8, 9], where  $\mathcal{G}$  synthesizes plausible content to generate the final right-view video  $\mathbf{X}_r$ .

$$\mathbf{X}_l = \mathcal{G}(\{\epsilon_t | t = 1, \dots, T\}, c), \quad (1)$$

$$\mathbf{X}_{l \rightarrow r}, \mathbf{M}_r = \text{Warp}_{l \rightarrow r}(\mathbf{X}_l, \mathbf{d}_l), \quad (2)$$

$$\mathbf{X}_r = \mathcal{G}(\{\epsilon_t | t = 1, \dots, T\}, c, \mathbf{X}_{l \rightarrow r}, \mathbf{M}_r). \quad (3)$$

**Spatial Video Generation.** Apple has introduced the concept of spatial video. Unlike conventional stereoscopic videos that provide fixed viewpoints, spatial video enables dynamic viewpoint changes, offering a more immersive and interactive viewing experience. To address disocclusions arising from viewpoint changes, we propose warping the monocular input video  $\mathbf{X}_l$  into multiple camera viewpoints (Eq. 4) surrounding the input monocular video

(Fig. 2, right) and employing a video diffusion model to hallucinate these disoccluded regions (Eq. 5). These videos maximally cover potential unknown areas, which are then optimized into a 4D representation for efficient stereoscopic novel view rendering (Eq. 6).

$$\mathbf{X}_{\text{warp}}, \mathbf{M} = \text{Warp}_{l \rightarrow m}(\mathbf{X}_l, \mathbf{d}_l), \quad (4)$$

$$\mathbf{X} = \mathcal{G}(\{\epsilon_t | t = 1, \dots, T\}, c, \mathbf{X}_{\text{warp}}, \mathbf{M}), \quad (5)$$

$$(\mathbf{X}_{l\_spatial}, \mathbf{X}_{r\_spatial}) := \mathbb{G}(\mathbf{X}). \quad (6)$$

Our framework comprises five technical components: (1) depth-based video warping (Sec. 3.2), (2) a novel *frame matrix* representation for video inpainting (Sec. 3.3), where the frame matrix representation significantly enhances both the semantic coherence across viewpoints and the temporal consistency across frames, (3) a disocclusion boundary re-injection mechanism for boundary refinement (Sec. 3.4), (4) a pipeline to extract stereoscopic video and spatial video from inpainted frame matrix (Sec. 3.5), and (5) an optional stereoscopic video super-resolution scheme (Sec. 3.6). Fig. 1 provides an overview of our pipeline.

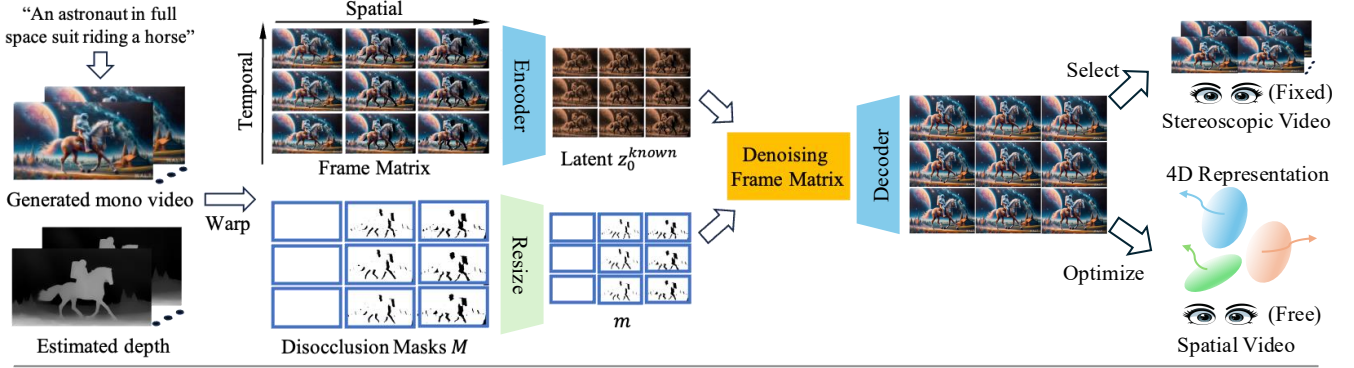
#### 3.2 Depth-Based Monocular Video Warping

We employ the depth estimation model of [7] to predict per-frame depth values, which are subsequently temporally smoothed to enhance consistency across the video frames. Specifically, consecutive depth frames are aligned using estimated optical flows from [53], while outliers in the predicted depths are suppressed via temporal convolution with a Gaussian kernel. The resulting RGB-D frames are then warped into pre-defined camera viewpoints. However, warped images often exhibit isolated pixels and entangled background and foreground (Fig. 14, left), which compromises visual quality [54]. To address these artifacts, we propose to warp RGB-D images onto multi-plane images [55], and then eliminate isolated pixels and cracks to obtain clean warped images for the subsequent generative inpainting.

**Multi-Plane Projection.** Given the RGB-D images, we warp them into a target camera view. Rather than projecting all pixels onto a single image plane and resolving occlusions via z-buffering, we partition the camera view space into  $N$  discrete planes  $\{\mathbf{X}_{\text{warp}_1}^{s1}, \dots, \mathbf{X}_{\text{warp}_K}^{s1}\}$  (where  $K = 4$  in our implementation), stratified according to near and far depth bounds. Each pixel is projected onto its closest image plane based on depth values. Binary masks  $\{\mathbf{M}_1^{s1}, \dots, \mathbf{M}_K^{s1}\}$  are used to identify occupied pixel positions on each plane. This multi-plane decomposition naturally separates foreground and background elements into distinct layers. Consequently, common warping artifacts, including isolated pixels and foreground-background entanglement, become significantly more tractable to address.

**Remove Isolated Points.** Due to depth inaccuracies near image content boundaries, boundary pixels are often warped to incorrect positions, resulting in isolated pixels (see red box in Fig. 14, left). We leverage the observation that isolated pixels typically have few or no neighboring pixels. For detection, we convolve each mask image  $\mathbf{M}_i^{s1}$  with a  $3 \times 3$  kernel and empirically classify pixels as isolated when their convolved values fall below 0.5. These isolated pixels are subsequently removed from both RGB images and masks, yielding the updated sets  $\{\mathbf{X}_{\text{warp}_1}^{s2}, \dots, \mathbf{X}_{\text{warp}_K}^{s2}\}$  and  $\{\mathbf{M}_1^{s2}, \dots, \mathbf{M}_K^{s2}\}$ .

**Fill Cracks.** The non-watertight nature of depth images often leads to cracks and holes in warped results, causing foreground-background confusion (e.g., visible road texture through the dog's



Details of Denoising Frame Matrix

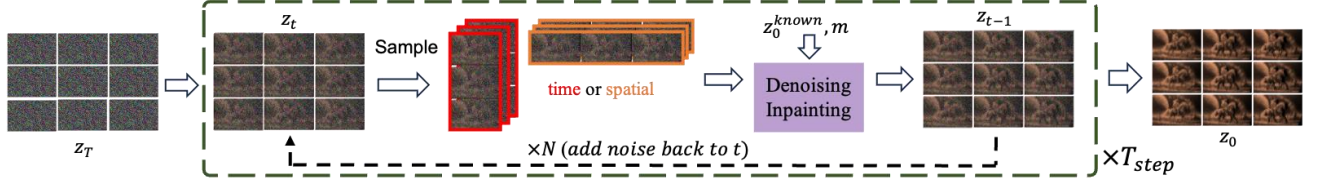


Fig. 1. **Overview – Top:** Given a text prompt, our method first employs a video generation model to generate a monocular video, which is warped into pre-defined camera views using estimated depth to form a *frame matrix* with disocclusion masks. Then, the disoccluded regions are inpainted by denoising the sampled frame sequences within the *frame matrix*. After denoising, we decode the clean latent *frame matrix* into RGB frames, where the 3D stereoscopic video is obtained via choosing the leftmost and rightmost columns. To generate spatial video, we optimize decoded frames into a 4D representation (e.g., 4D Gaussian) that supports continuous view changes. **Bottom:** Details of denoising *frame matrix*. We initialize the latent matrix  $z_T$  as random noise maps, and alternatively denoise them in sampled directions. Specifically, we extend the resampling mechanism [52, 9] to alternatively denoise temporal (column) sequences and spatial (row) sequences  $N$  times. Each time, row or column sequences are denoised and inpainted (Fig.3). By denoising along both spatial and temporal directions, we obtain an inpainted latent  $z_0$  which can be decoded into temporally smooth and semantically consistent sequences.

ear in Fig. 14, left). Building upon our isolated pixel removal approach, we detect cracks by convolving each mask  $M_i^{s^2}$  with a  $3 \times 3$  Gaussian kernel. In this paper, positions with no pixel values (0 in  $M_i^{s^2}$ ) but with values greater than 0.2 after convolution are empirically considered as cracks. The detected cracks are filled by local pixel interpolation, producing the final multi-plane images  $\{X_{warp\_1}^{s^3}, \dots, X_{warp\_K}^{s^3}\}$  and the corresponding masks  $\{M_1^{s^3}, \dots, M_K^{s^3}\}$ .

After processing all individual planes for artifacts, we composite them into the final output  $X_{warp}$  through back-to-front blending. The blending operation follows:

$$X_{warp} = X_{warp} \times (1 - M_i^{s^3}) + X_{warp\_i} \times M_i^{s^3}, \text{ for } i \text{ in } [K, \dots, 1], \quad (7)$$

where front plane content ( $i$  close to 1) naturally occludes back plane content ( $i$  close to  $K$ ). These warped images  $X_{warp}$  will be processed via video inpainting.

Nevertheless, monocular videos often contain partially visible objects, as shown by the coconut tree in Fig. 15 (a). When depth-based warping is directly applied to such cases, it results in incomplete objects in the warped images that cannot be adequately repaired through video inpainting. To resolve this issue, we employ video outpainting (implemented via single video denoising inpainting as described in Sec. 3.3) to extend the visible content, thereby providing more complete objects for subsequent warping. The outpainting padding size  $P$  is set equal to the maximum disparity value, computed as:

$$P = \frac{f \times b}{d_{\min}}, \quad (8)$$

where  $f$  is the focal length,  $b$  represents the binocular baseline, and  $d_{\min}$  is the minimum scene depth.

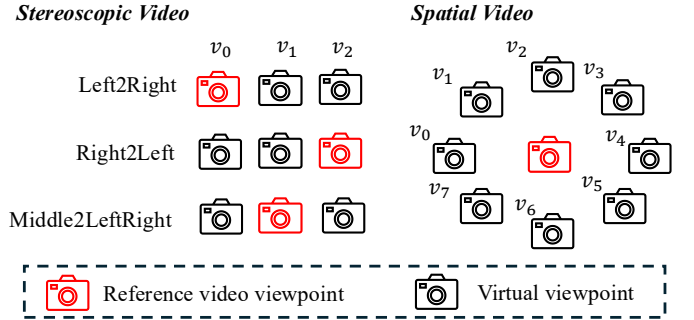


Fig. 2. **The setting of virtual camera viewpoints.** For stereoscopic video generation, virtual cameras are distributed along the interocular baseline. We use the left2right scheme by default, but other schemes are also viable. For spatial video generation, we position multiple virtual cameras around the reference viewpoint of the monocular video. To ensure circular consistency, the first and last columns of the *frame matrix* share the same first camera viewpoint.

### 3.3 Video Inpainting with Frame Matrix

The inpainting pipeline serves as a crucial component for maintaining both spatial/semantic coherence and temporal consistency in the output video. Although existing image inpainting methods [8, 9] offer a viable starting point, they inherently fail to preserve stability across both spatial and temporal dimensions. Therefore, we introduce a *frame matrix* representation, which addresses both issues. In the following, we first introduce the basic idea of single video denoising inpainting, followed by advanced frame matrix denoising inpainting.

**Single Video Denoising Inpainting.** Inspired by RePaint [9], we

extend the diffusion-based image inpainting to video inpainting. We use the video generation model  $\mathcal{G}$  (i.e., Zeroscope [5]) as our inpainting tool, which is a latent diffusion model consisting of a VAE encoder  $\mathcal{E}$ , a decoder  $\mathcal{D}$  and a latent denoiser  $\{\epsilon_\theta, \Sigma_\theta\}$ . First, the warped video is fed into the VAE encoder to obtain video latent features  $\mathbf{z}_0^{\text{known}} = \mathcal{E}(\mathbf{X}_{l \rightarrow r})$ . Accordingly, the image disocclusion masks  $\mathbf{M}_r$  are resized to match the resolution of encoded latent features, yielding latent disocclusion masks  $\mathbf{m}$ . The denoising process initializes with a random noisy latent map  $\mathbf{z}_T \sim \mathcal{N}(\mathbf{0}, \mathbf{I})$ . At each denoising step  $t$ , we denoise the latent map  $\mathbf{z}_t$  according to Eq. 10, sample a subsequent noisy latent map from  $\mathbf{z}_0$  following Eq. 9 and combine them with  $\mathbf{m}$  to obtain the  $\mathbf{z}_{t-1}$  using Eq. 11. We visualize the above steps in Fig.3 (b):

$$\mathbf{z}_{t-1}^{\text{known}} \sim \mathcal{N}(\sqrt{\bar{\alpha}_t} \mathbf{z}_0^{\text{known}}, (1 - \bar{\alpha}_t) \mathbf{I}), \quad (9)$$

$$\mathbf{z}_{t-1}^{\text{unknown}} \sim \mathcal{N}\left(\frac{1}{\sqrt{1 - \beta_t}} \left(\mathbf{z}_t - \frac{\beta_t}{\sqrt{1 - \bar{\alpha}_t}} \epsilon_\theta(\mathbf{z}_t, c, t)\right), \Sigma_\theta(\mathbf{z}_t, c, t)\right), \quad (10)$$

$$\mathbf{z}_{t-1} = \mathbf{m} \odot \mathbf{z}_{t-1}^{\text{known}} + (1 - \mathbf{m}) \odot \mathbf{z}_{t-1}^{\text{unknown}}, \quad (11)$$

where  $\bar{\alpha}_t$  represents the total noise variance and  $\beta_t$  denotes the one-step noise variance at timestep  $t$ . The denoising process employs two learned functions:  $\epsilon_\theta(\mathbf{z}_t, c, t)$  predicts the noise component, while  $\Sigma_\theta(\mathbf{z}_t, c, t)$  estimates the variance for the latent map at timestep  $t-1$ . The final inpainted sequence  $\mathbf{X}_r$  is obtained by decoding the denoised latent representation through  $\mathcal{D}(\mathbf{z}_0)$ . Considering that the VAE decoder cannot perfectly reconstruct warped pixels, we adopt Poisson Blending [56] to enhance the transition between generated and warped content in image space.

By applying the above video inpainting design to the warped images, we successfully hallucinate occluded regions while preserving known image content. Although the video diffusion model ensures temporal smoothness, the inpainted content on the warped view usually lacks semantic coherency with respect to the given reference view, as shown in the third column of Fig. 11. This is because we abandon the conditioning on the reference view and process the warped view independently.

**Frame Matrix Denoising Inpainting.** We introduce a novel representation—the *frame matrix*—designed to ensure consistent dynamic content generation across both space and time. As illustrated in Fig. 1 (top), the frame matrix is structured as a two-dimensional array of frames, where each row corresponds to multiple camera perspectives captured at the same timestamp, while each column represents a temporal sequence of frames recorded from a fixed camera viewpoint. Formally, the frame matrix can be defined as:

$$\mathbf{X} \equiv \begin{bmatrix} \mathbf{x}_{(:,0)} & \cdots & \mathbf{x}_{(:,V)} \end{bmatrix} \equiv \begin{bmatrix} - & \mathbf{x}_{(0,:)} & - \\ & \vdots & \\ - & \mathbf{x}_{(S,:)} & - \end{bmatrix},$$

where  $S$  and  $V$  denote the largest indices of time stamps and camera views, respectively. A spatial sequence (row)  $\mathbf{X}_{(s,:)}$  forms a video with camera motions, while a temporal sequence (column)  $\mathbf{X}_{(:,v)}$  forms a video with time-varying scene motions. Since the video generation model can generate temporally and semantically consistent dynamic or static videos, we adopt it to jointly denoise the rows and columns of *frame matrix*, ensuring spatial and temporal consistency. Finally, we can extract the immersive 3D video from it.

To initialize the frame matrix, we place  $V$  camera views with the same orientation of the reference view along the interocular

baseline for stereoscopic setups and distribute camera views surrounding the reference view for spatial setups (Fig. 2). Next, the depth-based warping method (Sec. 3.2) is employed to warp the reference video into these manually defined viewpoints and obtain  $\mathbf{X}_{\text{warp}} \equiv [\mathbf{X}_{(:,0)}, \mathbf{X}_{(:,1)}, \dots, \mathbf{X}_{(:,V)}]$  with disocclusion masks  $\mathbf{M}$ . The definition of the camera trajectory is flexible, depending on the demands.

The denoising process of frame matrix is similar to single video inpainting, we first encode the warped frame matrix into latent space as  $\mathbf{z}_0^{\text{known}} = \mathcal{E}(\mathbf{X}_{\text{warp}})$ , while resizing the disocclusion masks  $\mathbf{M}$  to obtain the latent mask matrix  $\mathbf{m}$ . We initialize the latent noise as  $\mathbf{z}_T \sim \mathcal{N}(\mathbf{0}, \mathbf{I})$ . As illustrated in Fig. 1 (Bottom), at each denoising timestep  $t$ , we extend the resampling mechanism [9] to alternatively denoise column sequences and row sequences  $N$  times. Each time, row or column sequences are denoised following Eq. 9-11 and then re-add noise back to the previous denoising timestep:

$$\mathbf{z}_t \sim \mathcal{N}(\sqrt{1 - \beta_{t-1}} \mathbf{z}_{t-1}, \beta_{t-1} \mathbf{I}). \quad (12)$$

---

#### Algorithm 1 Frame Matrix Denoising Inpainting

---

**Input:**  $\mathbf{z}_T \sim \mathcal{N}(\mathbf{0}, \mathbf{I})$ : Initial noisy latent maps

$\mathbf{z}_0$ : Initial clean latent maps

**for**  $t = T, \dots, 1$  **do**

**for**  $n = 1, \dots, N$  **do**

**if**  $n$  is odd **then**

      Denoise time sequences  $\{\mathbf{z}_{(:,v)t} | v = 0, \dots, V\}$ :

**for**  $v = 0, \dots, V$  **do**

$\mathbf{z}_{(:,v)t-1}^{\text{known}} \sim \mathcal{N}(\sqrt{\bar{\alpha}_t} \mathbf{z}_{(:,v)0}, (1 - \bar{\alpha}_t) \mathbf{I})$

$\mathbf{z}_{(:,v)t-1}^{\text{unknown}} \sim \mathcal{N}(\mu_\theta(\mathbf{z}_{(:,v)t}, c, t), \Sigma_\theta(\mathbf{z}_{(:,v)t}, c, t))$

$\mathbf{z}_{(:,v)t-1} = \mathbf{m}_{(:,v)} \odot \mathbf{z}_{(:,v)t-1}^{\text{known}} + (1 - \mathbf{m}_{(:,v)}) \odot \mathbf{z}_{(:,v)t-1}^{\text{unknown}}$

**end for**

**else**

      Denoise view sequences  $\{\mathbf{z}_{(s,:)} | s = 0, \dots, S\}$ :

**for**  $s = 0, \dots, S$  **do**

$\mathbf{z}_{(s,:)}^{\text{known}} \sim \mathcal{N}(\sqrt{\bar{\alpha}_t} \mathbf{z}_{(s,:)0}, (1 - \bar{\alpha}_t) \mathbf{I})$

$\mathbf{z}_{(s,:)}^{\text{unknown}} \sim \mathcal{N}(\mu_\theta(\mathbf{z}_{(s,:)t}, c, t), \Sigma_\theta(\mathbf{z}_{(s,:)t}, c, t))$

$\mathbf{z}_{(s,:)} = \mathbf{m}_{(s,:)} \odot \mathbf{z}_{(s,:)}^{\text{known}} + (1 - \mathbf{m}_{(s,:)}) \odot \mathbf{z}_{(s,:)}^{\text{unknown}}$

**end for**

**end if**

**if**  $n < N$  **then**

    Add back one noise step for resampling:

$\mathbf{z}_t \sim \mathcal{N}(\sqrt{1 - \beta_{t-1}} \mathbf{z}_{t-1}, \beta_{t-1} \mathbf{I})$

**end if**

**end for**

**end for**

---

Algorithm 1 presents detailed steps to denoise the *frame matrix* with spatial-temporal resampling. By denoising along these two directions alternatively, the spatial and temporal sequences will proceed toward a harmonic state.

**More Analysis of Frame Matrix.** (1) *High-level perspective.* In practical 3D stereoscopic video production, we typically record with two cameras to obtain the video sequences. Since both cameras capture the same scene, this means that gradually moving the position of the left camera towards the position of the right camera can also produce a coherent spatial-direction video. This principle



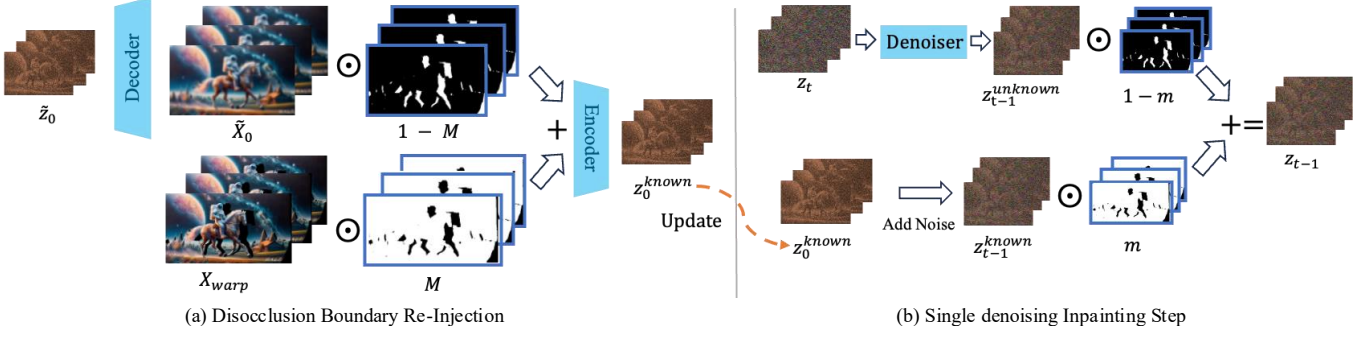


Fig. 3. **Denoising inpainting.** This figure explains the operations in the purple box of Fig.1. (a) We re-inject the generated content from a denoised latent  $\tilde{z}_0$  to update  $z_0^{\text{known}}$ , reducing its feature corruption on the disocclusion boundary. (b) A noisy latent  $z_t$  is denoised to  $z_{t-1}^{\text{unknown}}$ . We combine its disoccluded region with the noisy known region of  $z_{t-1}^{\text{known}}$  to obtain a complete denoised latent feature  $z_{t-1}$ .

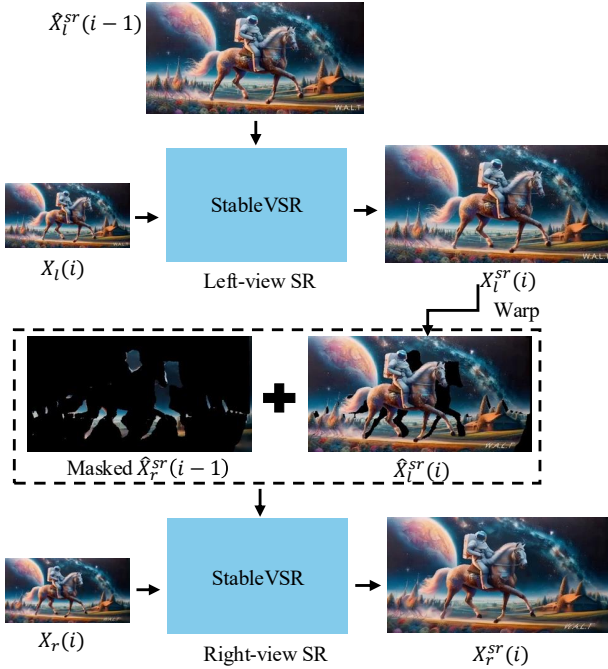


Fig. 4. **Stereoscopic video super resolution.** The left-view super resolution is conditioned on the previous upsampled frame, while the right-view super resolution is conditioned on both left-view and previous upsampled frames.

applies equally to 3D stereoscopic video generation: we must jointly consider both the temporal and spatial directions to ensure the generated perspectives properly represent the same scene. Furthermore, our experiments show that gradually expanding the inpainting region along the spatial direction yields more stable and reasonable results than attempting to inpaint large missing regions in a single step. This progressive approach better maintains consistency across viewpoints. (2) *Mathematical perspective.* Each frame  $z_{t-1}(i, j)$  in the latent frame matrix should be as consistent as the denoising results from both temporal and spatial directions. Mathematically:

$$L(i, j) = \|z_{t-1}(i, j) - z_{t-1}^T(i, j)\|_2 + \|z_{t-1}(i, j) - z_{t-1}^S(i, j)\|_2, \quad (13)$$

$$z_{t-1}^T = \Theta^T(z_t), \quad z_{t-1}^S = \Theta^S(z_t), \quad (14)$$

where  $\Theta$  is a pre-trained video diffusion model,  $\Theta^S$  and  $\Theta^T$  indicate denoising operations along the spatial and temporal

dimensions, respectively. Here,  $L$  is a quadratic Least-Squares (LS) problem where the solution closely approximates all diffusion samples  $z_{t-1}^S(i, j)$  and  $z_{t-1}^T(i, j)$ . In practice, we perform denoising in both spatial and temporal directions to approximate optimal results.

### 3.4 Disocclusion Boundary Re-Injection

Since most video generation models are using latent diffusion, the disoccluded regions of  $\mathbf{X}_{\text{warp}}$  will be propagated beyond the latent mask  $\mathbf{m}$  during VAE encoding (e.g., Zeroscope downsamples by  $8\times$ ), leading to corrupted latent features around  $z_0^{\text{known}}$ 's disocclusion boundary. This would result in artifacts in the final results (Fig. 12, left).

To address this issue, we propose a latent feature refinement strategy that re-injects denoised information into the disocclusion boundary features. Specifically, we predict denoised latent features [15] and decode them into a denoised video (Eq. 15). Next, we replace its unoccluded regions with warped pixels, producing a video that maintains faithfulness to the reference view while improving the disoccluded areas. Finally, re-encoding this composite video yields an updated latent representation  $z_0^{\text{known}}$  (Eq. 16), effectively mitigating boundary corruption:

$$\tilde{\mathbf{X}}_0 = \mathcal{D}(\tilde{\mathbf{z}}_0), \text{ where } \tilde{\mathbf{z}}_0 = \frac{1}{\sqrt{\alpha_t}} (z_t - \sqrt{1 - \alpha_t} \epsilon_\theta(z_t, c, t)), \quad (15)$$

$$z_0^{\text{known}} = \mathcal{E}(\mathbf{M} \odot \mathbf{X}_{\text{warp}} + (1 - \mathbf{M}) \odot \tilde{\mathbf{X}}_0). \quad (16)$$

This improved  $z_0^{\text{known}}$  will be used in Eq. 9 for the next iteration.

### 3.5 Extract Stereoscopic and Spatial Videos

After denoising inpainting the latent frame matrix, we decode it into multi-view videos  $\mathbf{X} = \mathcal{D}(\mathbf{z}_0)$ , where the stereoscopic and spatial videos can be extracted.

**Extract Stereoscopic Video.** Since stereoscopic videos provide a fixed viewpoint when observing a scene, we select the leftmost and rightmost columns from the frame matrix ( $\mathbf{X}_l, \mathbf{X}_r$ ) to represent observations of the left and right eyes.

**Extract Spatial Video.** The output frame matrix, composed of multi-view videos, is a discrete observation of the scene and cannot support continuous view synthesis required by spatial videos. To address this, we optimize the generated multi-view observations into a 4D representation, enabling continuous and consistent

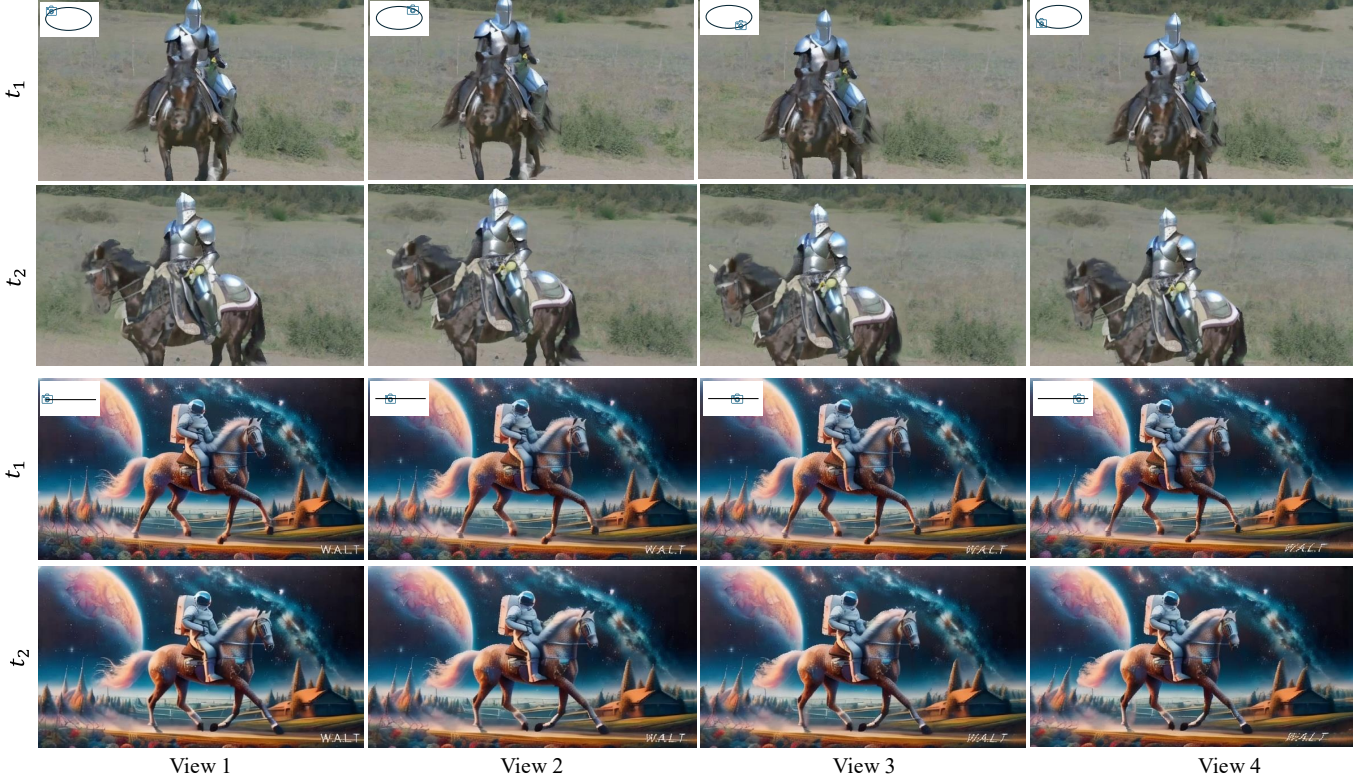


Fig. 5. **Frames sampled from denoising inpainted frame matrix.** Each row represents a video with camera motions at a fixed timestamp. Each column is a video, recording the scene motion from a camera viewpoint.

stereoscopic view synthesis. Considering the rendering efficiency, we choose the *Deformable Gaussian Splatting (DGS)* [10] as our backbone, which takes posed images as inputs and learns a set of 3D Gaussians  $G(\mathbf{p}, \mathbf{r}, \mathbf{s}, \sigma, \mathbf{c})$  in a canonical space, associated with time-dependent offsets  $(\delta_{\mathbf{p}}^t, \delta_{\mathbf{r}}^t, \delta_{\mathbf{s}}^t)$ . Here,  $\mathbf{p}$  denotes the center positions,  $\sigma$  indicates opacity,  $\mathbf{c}$  represents view-dependent appearances, while the quaternion  $\mathbf{r}$  and the scaling  $\mathbf{s}$  define the shape of Gaussian primitives.

Specifically, we back-project the first RGB-D frame ( $t = 0$ ) of the reference video into the 3D canonical space, which serves as the initial state for the 3D Gaussian primitives. To model dynamic motions, the 3D Gaussian primitives are deformed  $G(\mathbf{p} + \delta_{\mathbf{p}}^t, \mathbf{r} + \delta_{\mathbf{r}}^t, \mathbf{s} + \delta_{\mathbf{s}}^t, \sigma, \mathbf{c})$  based on time-dependent offsets, which are predicted using an *MLP* with given timestamp  $t$  and positions  $\mathbf{p}$  of 3D Gaussians as inputs:

$$(\delta_{\mathbf{p}}^t, \delta_{\mathbf{r}}^t, \delta_{\mathbf{s}}^t) = \text{MLP}(\gamma(\text{sg}(\mathbf{p})), \gamma(t)), \quad (17)$$

where  $\text{sg}$  indicates a stop-gradient operation,  $\gamma$  denotes the positional encoding. During the optimization process, the deformed 3D Gaussians at timestamp  $t$  are rasterized [30] into 2D images under pre-defined camera viewpoints (row of *frame matrix*) and compared with generated images  $\mathbf{X}$  at timestamp  $t$ . This optimization is guided by a combination of  $\mathcal{L}_1$  loss and *LPIPS* loss, ensuring both accuracy and high-quality rendering:

$$\mathcal{L} = \lambda_1 \times \mathcal{L}_1 + \lambda_2 \times \text{LPIPS}. \quad (18)$$

To improve robustness, we further augment this optimization process by randomly sampling viewpoints within the circular trajectory (Fig. 2) for supervision, where unknown regions are excluded from loss computation. Following [30], adaptive density

control is employed, but we disable the pruning operation in practice to obtain renderings with higher quality.

Unlike the vanilla *DGS*, our optimization process circumvents the need for challenging cross-time camera pose estimation by assuming camera poses across timestamps are fixed and modeling each Gaussian as a dynamic entity. Temporal coherence is maintained through predicted inter-frame offsets, while multi-view imagery provides constraints for the 3D geometries at each timestamp.

### 3.6 Stereoscopic Video Super Resolution

We develop a stereo video super-resolution framework built upon a pre-trained monocular video super-resolution model [57] (denoted as  $\mathcal{SR}$ ). As illustrated in Fig. 4, our pipeline first processes the left-view video sequence  $\mathbf{X}_l(i)$  through the original  $\mathcal{SR}$  architecture:

$$\mathbf{X}_l^{sr}(i) = \mathcal{SR}(\mathbf{X}_l(i), \hat{\mathbf{X}}_l^{sr}(i-1)), \quad (19)$$

where  $\hat{\mathbf{X}}_l^{sr}(i-1)$  represents the temporally aligned version (via optical flow) of the previous upsampled frame, which serves as a temporal condition to ensure inter-frame consistency. In contrast, the right-view upsampling incorporates both temporal condition from  $\hat{\mathbf{X}}_r^{sr}(i-1)$  and cross-view condition from  $\hat{\mathbf{X}}_l^{sr}(i)$  to maintain both temporal stability and stereo coherence:

$$\mathbf{X}_r^{sr}(i) = \mathcal{SR}(\mathbf{X}_r(i), \text{Mix}(\hat{\mathbf{X}}_l^{sr}(i), \hat{\mathbf{X}}_r^{sr}(i-1))), \quad (20)$$

where *Mix* denotes an operation that replaces regions in the upsampled right-view frame  $\hat{\mathbf{X}}_r^{sr}(i-1)$  with their warped counterparts from the upsampled left-view frame  $\hat{\mathbf{X}}_l^{sr}(i)$ .





Fig. 6. **Qualitative comparisons on stereoscopic generation.** The first row is left-view images, while the others show the synthesized right-view images. The video inpainting methods E2FGVI and ProPainter tend to generate blurry content in disoccluded regions. RoDynRF and DynIBaR cannot generate occluded content and produce results with artifacts.

## 4 EXPERIMENTS

### 4.1 Implementation Details

**Datasets.** To validate our method’s effectiveness, we conduct experiments with a variety of recent video generation models, including Sora [1], Lumiere [11], WALT [12], and Zeroscope [5]. These models generate diverse videos from a wide range of input text prompts, encompassing a broad spectrum of subjects, including humans, animals, buildings, and imaginary content.

**Inference and optimization Details.** 1) *Stereoscopic video.* To achieve realistic 3D effects, we first normalize the predicted depth values from [7] to the range (1, 10) and set the interocular baseline to 0.07 meter. Our multi-view setup consists of 6 virtual cameras uniformly distributed between the left and right views, with each camera generating a corresponding warped video sequence. Due to computational constraints of the Zeroscope model, we limit our experiments to 16-frame video sequences. For the denoising process, we adopt the DDPM framework [15] with  $T = 1000$



total timesteps and perform denoising in 50 steps (that is, jumps of 20 timesteps per step). Following the RePaint strategy [9], we implement an adaptive resampling schedule: During the initial coarse denoising phase (steps 50–25), we apply 8 resampling iterations per step to establish coherent structures in disoccluded regions. In the refinement phase (steps 25–0), we reduce to 4 resamples per step and focus denoising exclusively on the right view for computational efficiency. 2) *Spatial video*. Different from the implementation of stereoscopic video, we place 16 cameras on a circular trajectory, with the radius set as 0.07 meters, surrounding the reference viewpoint and denoise the entire frame matrix to obtain multi-view videos. When optimizing the 4D Gaussian,  $\lambda_1$  and  $\lambda_2$  are set to 1.0 and 0.15 respectively, and the total number of optimization iterations is 20000. For training efficiency, the *LPIPS* loss is evoked after 13000 iterations.

**Baselines.** We first evaluate our method against two families of approaches: video inpainting and novel view synthesis from a monocular video. For video inpainting approaches, we produce right views through depth-guided warping identical to our pipeline, then process them with state-of-the-art inpainting methods: ProPainter [49] and E2FGVI [50]. For novel view synthesis methods, we compare our results with RoDynRF [3] and DynIBaR [2], which optimize scene representations relying on camera poses. To ensure a fair comparison, given the differing 3D scales between their reconstructed scenes and our estimated depth, we align their rendering baseline with ours by matching median foreground disparities in the resulting disparity maps. We also include comparisons with single-image view synthesis approaches, such as SVM [32] and AdaMPI [33], which fail to leverage temporal information. Next, we are also aware of approaches trained on dedicated datasets that directly produce the right view given the left view, like Deep3D [51]. However, it does not generalize well to generated videos, especially those in non-realistic styles. Finally, we compare with the concurrent work Free4D [58] that generates 4D scene based on the geometric structure from MonST3R [59].

## 4.2 Qualitative Results

**Frames in Generated Frame Matrix.** In Fig. 5, we sample frames across different camera viewpoints and timestamps in the inpainted frame matrix. Each row represents a video with camera motions at a specific timestamp; the corresponding camera positions are displayed in the top left corner. Each column contains frames at different timestamps, as observed from a camera viewpoint. The results exhibit spatial-temporal coherence in both the foreground and background components.

**Qualitative Comparisons on Stereoscopic Generation.** We present qualitative comparisons in Fig. 6. Existing video inpainting methods exhibit a common limitation: the generated content in disoccluded regions (*e.g.*, the knight’s arm, horse’s tail, corgi’s face, and turtle’s head) often appears blurry, likely due to training on limited datasets. On the other hand, novel view synthesis methods struggle with unstable camera pose estimation (*e.g.*, DynIBaR’s failure on certain videos). While these methods excel at reconstructing visible content from monocular video, they are typically poor at synthesizing novel contents in the disoccluded regions that are not observed in any frames (*e.g.*, ghost effect near the boundary in the RoDynRF result on the corgi example). Our approach leverages the generative power of video diffusion

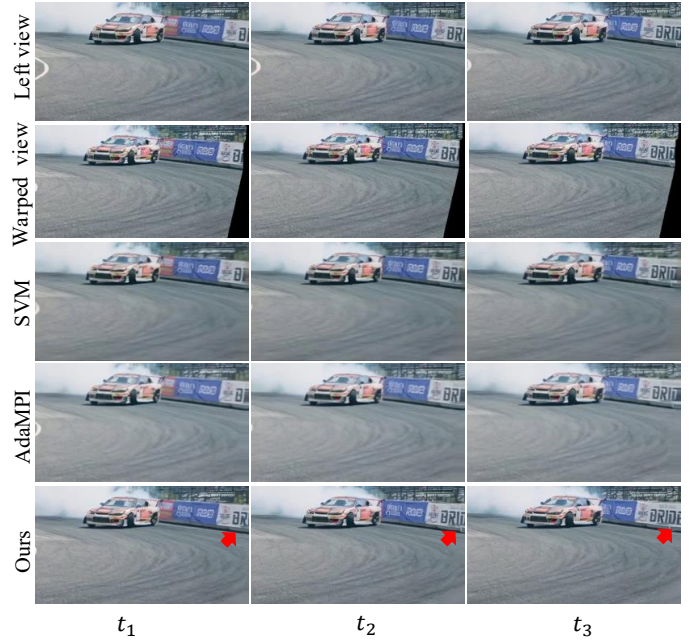


Fig. 7. **Modeling temporal relationships.** Our method leverages future information to inpaint disoccluded regions. Please note that the generated character “R” at time  $t_1$  matches the left-view character at time  $t_2$ . Single-image view synthesis methods (SVM and AdaMPI) produce temporally inconsistent results.

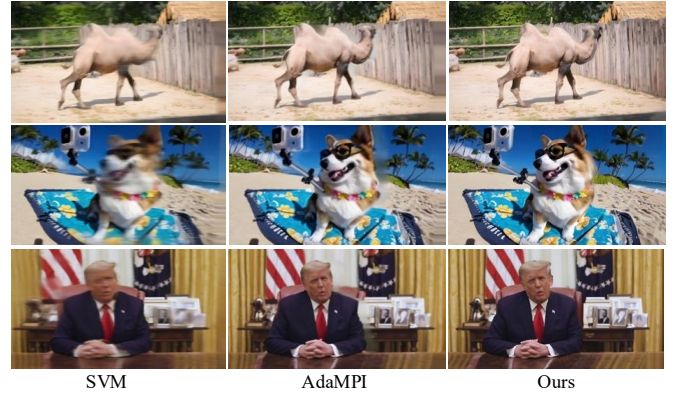


Fig. 8. **More comparisons with single-image view synthesis.** SVM and AdaMPI tend to produce blurry results in disoccluded regions.

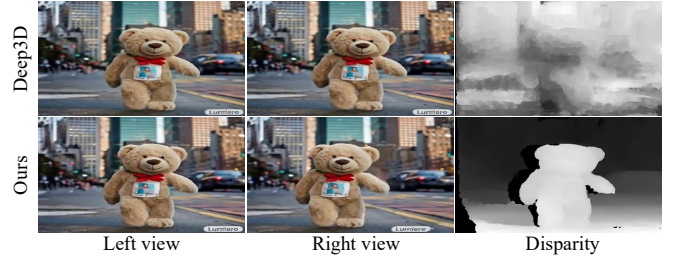


Fig. 9. **Results of Deep3D.** The predicted disparity map [60] of Deep3D is blurry, indicating its weak 3D effect. Moreover, Deep3D can only generate fixed binocular videos and does not provide the flexibility of changing the stereo baseline.

models trained on large-scale datasets and eliminates the need for input camera poses. As demonstrated in the last row of Fig. 6, our method generates high-quality content in various scenarios and consistently exceeds baselines.

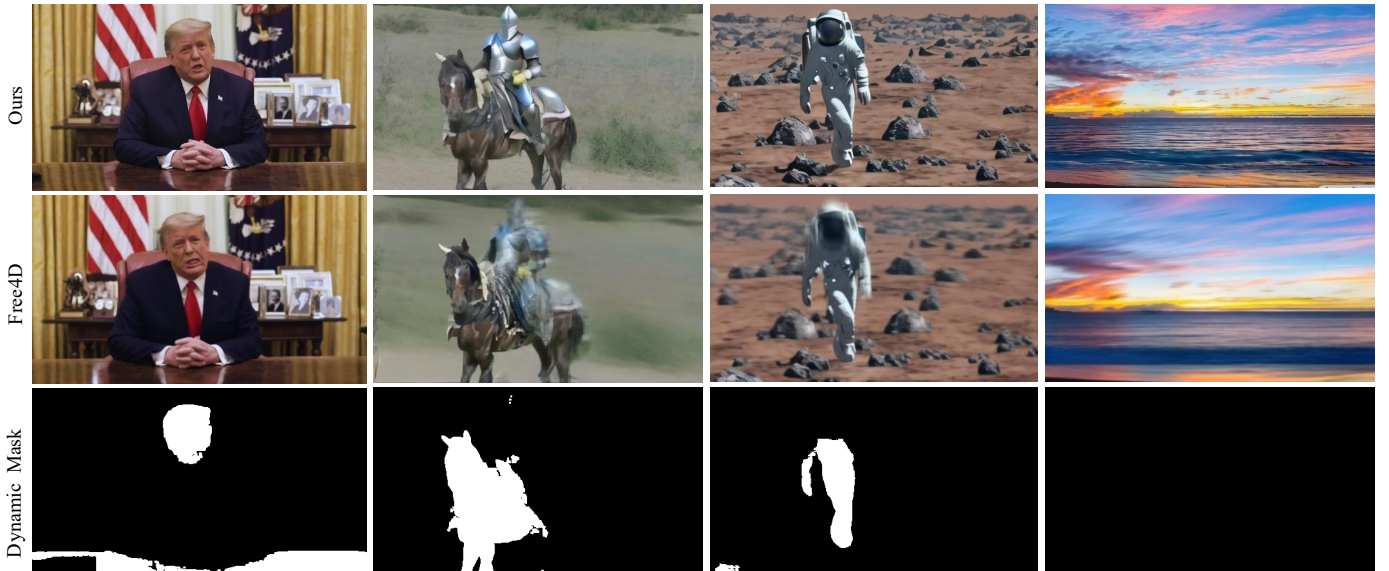


Fig. 10. **Qualitative comparisons on spatial generation.** We evaluate the spatial generation capability by comparing rendered images from the generated 4D scenes. Our approach outperforms Free4D in terms of image quality and sharpness, especially on scenes with complex motions, such as the running horse and non-rigid water flowing, where Free4D produces blurry results. Additionally, we display the dynamic mask, a key component of Free4D, predicted by MonST3R, which needs further fine-tuning to accurately represent the dynamic regions in a large variety of scenes with complex motions.

TABLE 1

**Human perception.** This table reports the results of human perception experiments as mean (std). Our method outperforms all other training-free baselines on all metrics, excluding Deep3D, which is fine-tuned on private stereo videos. Deep3D achieves slightly better video quality and consistency, but significantly sacrifices the stereo effect and overall experience.

	E2FGVI	ProPainter	RoDynRF	DynIBaR	Deep3D	Ours
Stereo Effect $\uparrow$	4.79 (1.08)	<u>4.81</u> (1.13)	2.97 (1.34)	1.86 (1.25)	2.27 (1.40)	<b>5.24</b> (0.94)
Temporal Consistency $\uparrow$	4.74 (1.33)	4.74 (1.22)	3.35 (1.66)	1.89 (1.33)	<b>5.46</b> (1.20)	<u>5.15</u> (1.22)
Image Quality $\uparrow$	4.42 (1.27)	4.38 (1.28)	2.84 (1.60)	1.67 (1.07)	<b>5.27</b> (1.31)	<u>5.12</u> (1.33)
Overall Experience $\uparrow$	<u>4.67</u> (1.04)	4.66 (1.09)	2.92 (1.43)	1.72 (1.06)	3.88 (0.96)	<b>5.35</b> (0.99)

TABLE 2

**Quantitative comparisons on stereoscopic generation.** We show the semantic consistency using CLIP feature similarity [61] between the left and right views. Additionally, the quality of generated videos is measured by aesthetic score [62], DOVER [63], and FVD [64]. Our method outperforms previous methods as well as ablated cases.

Method	E2FGVI	ProPainter	RoDynRF	DynIBaR	SVM	AdaMPI	Ours - FM	Ours - DBR	Ours
CLIP $\uparrow$	94.34	95.29	96.03	93.24	92.11	93.61	95.81	95.60	<b>96.44</b>
Aesthetic $\uparrow$	5.06	5.07	4.97	4.66	4.87	4.78	5.25	5.18	<b>5.27</b>
DOVER $\uparrow$	0.547	0.535	0.352	0.365	0.215	0.245	0.565	0.560	<b>0.584</b>
FVD $\downarrow$	638	606	727	1208	784	718	614	699	<b>599</b>

TABLE 3

**Quantitative comparisons on spatial generation.** We render videos from established 4D scenes and measure the quality of rendered videos using the aesthetic score, Dover, and FVD. Our method outperforms Free4D.

Method	Aesthetic $\uparrow$	DOVER $\uparrow$	FVD $\downarrow$
Free4D	4.97	0.371	1129
Ours	<b>5.18</b>	<b>0.567</b>	<b>518</b>

Without using input camera poses, single-image view synthesis methods can produce stereoscopic videos by processing each frame individually. We compare our approach with SVM [32] and AdaMPI [33], presenting results at different timestamps in Fig. 7. At a specific timestamp (e.g.,  $t_1$ ), both SVM and AdaMPI produce blurry artifacts near the character “B”, whereas our method recon-

structs a sharp character “R”. This enhancement stems from our framework’s ability to aggregate multi-frame information (e.g., leveraging the left-view frame at  $t_2$ ). Furthermore, AdaMPI and SVM exhibit temporal inconsistencies due to their per-frame processing paradigm; for example, the region adjacent to “B” varies between  $t_1$  and  $t_2$ . In contrast, our video generation model enforces temporal coherence, ensuring alignment of synthesized characters with the left-view sequence. Additional comparative results are provided in Fig. 8.

Furthermore, we compare our method with Deep3D [51], which is trained on private stereoscopic videos. In Fig. 9, we visualize 3D effects by predicting the disparity map from generated stereoscopic pairs using STTR [60]. The vague disparity map of Deep3D in the third column demonstrates its weak stereo effects, while our method displays a clear order of foreground

and background content with smooth depth changes. Moreover, Deep3D does not support manually modifying the disparity map or changing the stereo baseline to achieve different stereo effects.

**Qualitative Comparisons on Spatial Generation.** In Fig. 10, we display rendered images from optimized 4D scenes. Our method outperforms Free4D [58] in terms of rendering quality and sharpness. Since Free4D employs MonST3R’s results as the geometry initialization, which reconstructs dynamic and static content in the 4D scene separately, we show the output dynamic masks (Fig. 10, third row), where white represents dynamic regions. From these dynamic masks, we observed that precisely segmenting the dynamic regions remains difficult, especially in scenes with complex motions, such as the fast-moving horse and the non-rigid motion of water flowing. Consequently, the failure to separate dynamic and static regions results in blurred reconstruction in Free4D. In contrast, our method circumvents predicting dynamic regions; instead, we treat each Gaussian primitive as a potential dynamic entity and learn a time-dependent deformation offset. Moreover, Free4D’s performance degrades when the input video contains camera motions. For example, the case of Trump with a fixed camera viewpoint performs better than other cases. This is because camera motions exaggerate task difficulty, and the temporal replacement operation in Free4D is not suitable for input videos with viewpoint changes. Video comparisons are displayed on our project page, where our method showcases temporally consistent results.

### 4.3 Quantitative Results

This section presents comprehensive quantitative comparisons with state-of-the-art baseline methods. Our evaluation framework combines both subjective and objective assessment metrics: (1) a rigorously designed user study evaluating multiple quality dimensions of the generated stereoscopic videos, (2) an objective metric based on the CLIP model that quantifies semantic alignment between left and right views, and (3) three established metrics measuring the quality of generated videos.

**Human Perception.** To evaluate perceived visual quality, we conducted a controlled user study involving 20 participants (9 female, age  $\mu = 33, \sigma = 6.2$ ). Using a VR headset, each participant assessed five randomly selected videos (from a pool of 20) generated by all five methods. The evaluation covered four key dimensions: stereo effect, temporal consistency, image quality, and overall experience, measured using a 7-point Likert scale [65]. A total of 435 evaluations (DynIBaR failed to generate 13 videos) were counterbalanced and randomly shuffled. We also included a training session to eliminate novelty effects. Results are summarized in Table 1, our method outperforms other view synthesis and video inpainting baselines in measured metrics. Deep3D achieves good video quality and consistency via slightly modifying the input reference video, which significantly sacrifices stereo effects (demonstrated by Fig. 9) and overall experience.

**Semantic Consistency.** To further evaluate view consistency, we introduce a semantic alignment metric based on pre-trained CLIP features [66]. For each stereoscopic video, we extract feature embeddings from both left and right views, then compute their similarity using the distance metric proposed in [67]. As demonstrated in Table 2, our method achieves superior semantic consistency with a score of 96.44, outperforming baseline approaches.

**Video Quality Assessment.** We evaluate video quality using three established metrics aligned with human judgment: (1) the aesthetic score  $\uparrow$  [62], (2) DOVER  $\uparrow$  [63], and (3) FVD  $\downarrow$  [64]. In Table 2, our approach in stereoscopic generation achieves the best performance (5.27, 0.584, and 599), aligning with the conclusion from the user study experiment in Table 1. When evaluating spatial generation, we randomly sample six viewpoints and render videos from the optimized 4D scenes. We report the measured video quality in Table 3, where our approach outperforms Free4D on all metrics (5.18 *vs.* 4.97, 0.567 *vs.* 0.371, and 518 *vs.* 1129).

### 4.4 Ablation Studies

**Effects of Frame Matrix.** Fig. 11 demonstrates the critical role of the frame matrix in maintaining semantic consistency between left and right views. When the frame matrix is disabled, the warped images’ disoccluded regions (e.g., the man’s hair and horse’s head) exhibit inconsistent content despite the diffusion model’s strong generative capabilities. This is quantitatively confirmed in Table 2, where disabling the frame matrix reduces the CLIP Score from 96.44 to 95.81. Thanks to the frame matrix that provides essential constraints from neighboring frames, ensuring both foreground and background content in disoccluded regions remain plausible and coherent.

**Effects of Disocclusion Boundary Re-Injection.** Fig. 12 demonstrates the importance of updating unoccluded latent features for achieving high-quality results. When this update step is omitted, the disoccluded region is inpainted with unnatural textures that cannot blend well with the surrounding warped content. In contrast, our approach with feature updating produces seamless content integration, as evidenced by both visual results and quantitative metrics. Specifically, Table 2 shows that disabling feature updates leads to a measurable degradation in performance, with the aesthetic score dropping from 5.27 to 5.18. Additionally, this boundary re-injection design demonstrates broader applicability beyond video inpainting, as evidenced by its effectiveness in improving existing image inpainting approaches. Fig. 13 shows consistent quality improvements when applied to methods like blended latent diffusion [8], where the technique helps reduce artifacts near inpainting boundaries.

**Effects of Handling Isolated Pixels and Cracks.** Fig. 14 (left) reveals significant artifacts in the warped images, including isolated points and visible cracks where the foreground ear improperly blends with the gray road background. Crucially, these artifacts persist in the final generated output without our proposed processing. After implementing our warping framework described in Section 3.2, the results demonstrate marked improvement, as shown in Fig. 14 (right). Our approach successfully eliminates these warping artifacts while maintaining both foreground and background structural integrity.

**Effects of Handling Partially Observed Objects.** Fig. 15 (a) shows a partially observed coconut tree and its depth-based warping results. Since regions belonging to the unobserved trunk are occupied by the background sky, these regions cannot be modified by the following video inpainting, leading to an incomplete coconut tree in the final output. To address this, we propose to outpaint the video (regions outside the red box), which provides a more complete coconut tree for warping and inpainting, thereby preserving correct occlusion relationships, as shown in Fig. 15 (b).



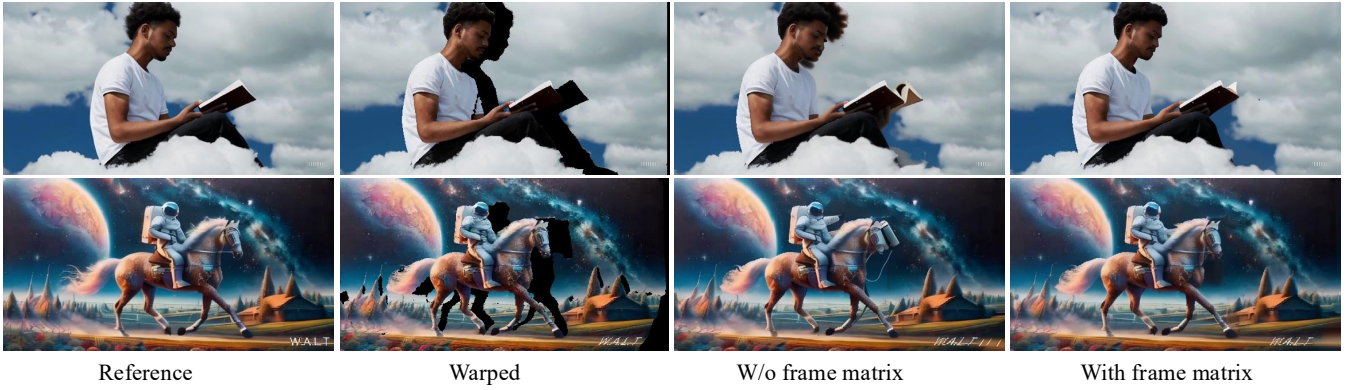


Fig. 11. **Semantic coherence across views.** Warp the reference frame into the target view and set the occluded areas to black. Without using the frame matrix, the generated content does not match the reference image, such as the book and the horse’s face. With the frame matrix, the inpainted content is more semantically reasonable across views.

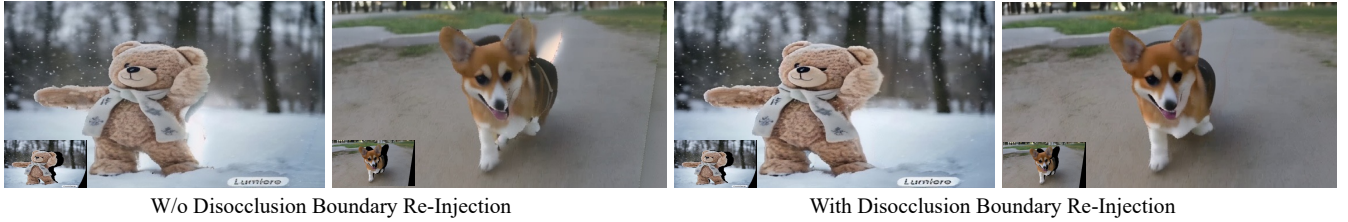


Fig. 12. **Disocclusion boundary re-injection.** Without disocclusion boundary re-injection for latent feature updating, the inpainted images usually contain artifacts. The warped image is shown at bottom left.

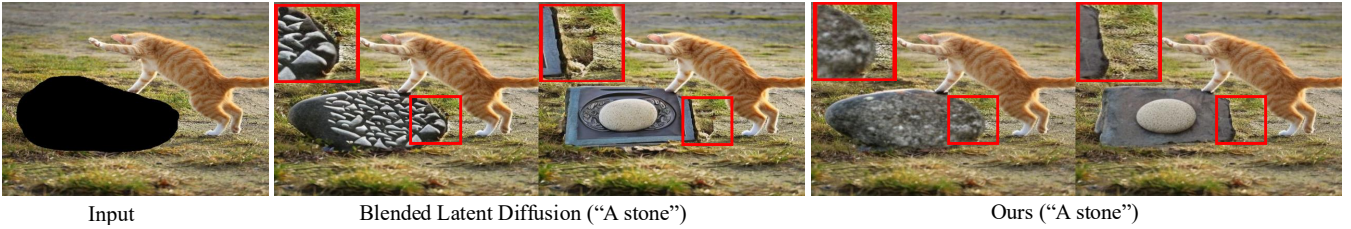


Fig. 13. **Disocclusion boundary re-injection in image inpainting.** Our approach (blended latent diffusion + disocclusion boundary re-injection) provides a smoother transition between original and inpainted content, such as the grassland.

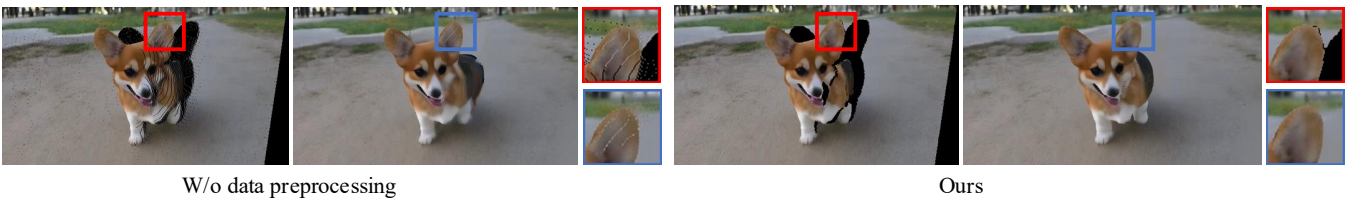


Fig. 14. **Isolated points and cracks.** Left: without handling isolated points and entangled foreground and background (the gray road is observed through cracks) in warped images, these artifacts remain in the final results. Right: our results are clean.

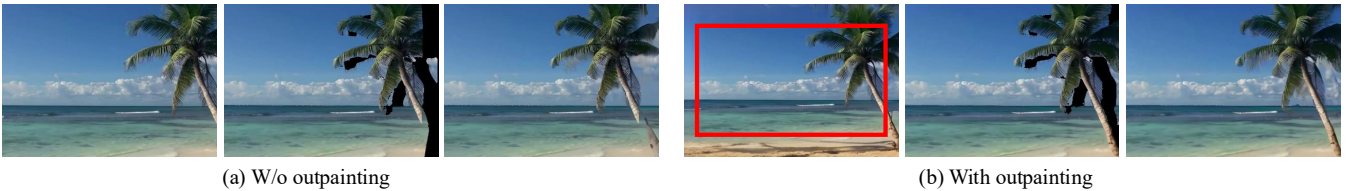


Fig. 15. **Partially observed object.** (a) The coconut tree is incomplete in the video. Using depth-based warping causes wrong occlusion relationships, where the background sky occupies regions belonging to the trunk. This problem cannot be fixed by video inpainting. (b) We outpaint the input video (regions outside the red box), thus providing a more complete coconut tree for correct warping and inpainting.

**Effects of Stereoscopic Video Super Resolution.** In Fig. 16, we presents our video super-resolution results. While indepen-

dent upsampling of left and right views fails to maintain cross-view consistency (evident in the zoomed-in regions), our method



Fig. 16. **Stereoscopic super resolution.** Independent upsampling of left-view and right-view videos often leads to binocular inconsistency, as demonstrated in the first two columns. Our method maintains cross-view consistency by explicitly coupling the binocular information during the upsampling process.



Fig. 17. **Different number of cameras used.** Artifacts arise when the number of cameras between left and right views is too small to exceed the capability of handling abrupt changes of video generation models.

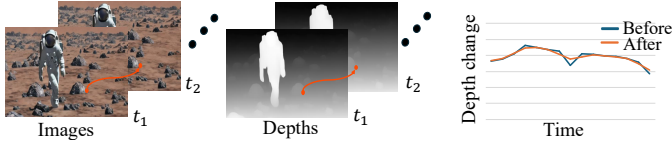


Fig. 18. **Temporal depth smoothing.** We track a pixel’s depth values across frames and visualize the depth changes. By applying smoothing operations, the depth changes more smoothly.

preserves stereo coherence by explicitly establishing inter-view connections during the upsampling process.

**Effects of Temporal Depth Smoothing.** In Fig. 18, we track a pixel across video frames and display its depth changes with and without using our depth smoothing operation. From Fig. 18 (right), our approach effectively stabilizes depth changes across frames.

**Number of Cameras Used.** When generating stereoscopic videos, we gradually reduce the number of cameras between the left and right views and show results in Fig. 17. Artifacts (e.g., the fifth leg) tend to arise when the number of cameras is fewer than four in this horse case, as a limited number of cameras can lead to rapid changes between video frames that exceed the capabilities of current video generation models.

**Different Stereo Baselines.** Fig. 19 demonstrates the impact of stereo baseline on inpainting difficulty and output quality. The performance degrades with the increasing baseline, and our method maintains robustness up to approximately 20cm (with scene depth normalized to 1.0–10.0 meters). This operational range comfortably accommodates typical viewing scenarios, as it substantially exceeds the average human inter-pupillary distance of 5–7cm. The results confirm our method’s practical suitability for generating stereoscopic content across realistic viewing conditions.

**Stereo Effects Visualization.** To further verify the quality of stereo effects, we compute more disparity maps from our generated stereo videos utilizing STTR [60]. Fig. 20 (a) demon-

strates that our results produce sharp disparity maps with clear foreground-background separation, confirming plausible 3D perception effects. The method achieves this via maintaining strong consistency with the input monocular depth - a natural consequence of our warping-based approach and the mask-aware diffusion model’s tendency to preserve known pixels. This is validated in Fig. 20 (b), comparing monocular (first column) and binocular (second column) estimated disparity maps. The small average difference of 0.63 pixels (last column) indicates excellent geometry preservation.

**Results at Different Denoising Time Steps.** In Fig. 21, we show results at different denoising time steps to enhance the understanding of the denoising inpainting process. Without the disocclusion boundary re-injection, noticeable artifacts gradually appear during the denoising process. In contrast, our method can gradually fill in disoccluded regions with harmonious content.

**Diverse Outputs.** As illustrated in Fig. 22, the output is non-unique since disoccluded regions can be plausibly synthesized with varying content—for instance, as cliffs or trees.

## 5 CONCLUSION

We present a comprehensive system for stereoscopic and spatial video generation that combines a video diffusion model with our novel *frame matrix* inpainting scheme and pose-free 4D optimization. As video generation technology advances rapidly, our work addresses the critical gap between monocular and immersive video synthesis capabilities. Specifically, we demonstrate that our *frame matrix* formulation and 4D optimization achieve state-of-the-art performance in generative stereoscopic and spatial videos and can be easily integrated into existing video diffusion frameworks.

**Limitations and Discussions.** While our results demonstrate the feasibility of generating 3D immersive videos using pre-trained monocular video diffusion models, several challenges remain. First, our study is limited to short video clips due to the inherent constraints of current video diffusion architectures and





Fig. 19. **Different stereo baselines.** Unnatural artifacts begin to appear as the baseline expands. Our method performs well for stereoscopic video generation where the baseline is usually less than 7cm.



Fig. 20. **3D effects visualization.** (a) The generated stereo results are used for predicting disparity maps [60]. The clear distinction between foreground and background content indicates reasonable 3D effects. (b) Disparity maps are estimated from monocular and binocular images. The discrepancy map on the right side demonstrates their consistency.

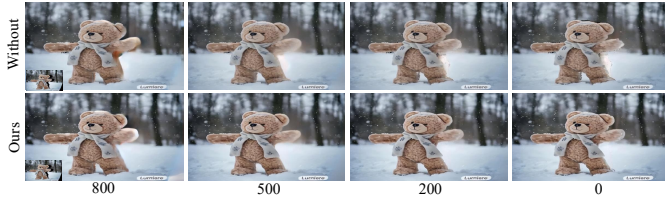


Fig. 21. **Results at different denoising timesteps.** Without the use of disocclusion boundary re-injection, artifacts persist throughout the denoising process. In contrast, our method gradually fills in disoccluded regions with harmonious content.



Fig. 22. **Diverse outputs.** The disoccluded regions can be generated with different content.

memory limitations, which typically generate only a few seconds of footage. Likewise, similar issues exist in 4D optimization, where modeling long-range scene motion remains a challenge. This limitation could potentially be addressed through sequential generation of overlapping shorter clips to construct longer videos. Second, our method relies on depth estimation models that may encounter difficulties with thin structures or object boundaries. In practice, we observe that depth consistency improves significantly when using models trained on large-scale datasets containing images extracted from the same scene and videos, and our flow-based smoothing operation further alleviates occasional depth flickering. For enhanced performance, future work could explore fine-tuning video generation models with synthetic video depth

data and predicting metric depths for physically correct geometries. Importantly, our framework is agnostic to the specific depth estimation method and can naturally benefit from advances in this area. Third, our method currently does not support large-view changes, such as back and front views, due to the weak multi-view priors.

## REFERENCES

- [1] T. Brooks, B. Peebles, C. Holmes, W. DePue, Y. Guo, L. Jing, D. Schnurr, J. Taylor, T. Luhman, E. Luhman, C. Ng, R. Wang, and A. Ramesh, “Video generation models as world simulators,” 2024. [Online]. Available: <https://openai.com/research/video-generation-models-as-world-simulators>
- [2] Z. Li, Q. Wang, F. Cole, R. Tucker, and N. Snavely, “Dynibar: Neural dynamic image-based rendering,” in *Proceedings of the IEEE/CVF Conference on Computer Vision and Pattern Recognition*, 2023, pp. 4273–4284.
- [3] Y.-L. Liu, C. Gao, A. Meuleman, H.-Y. Tseng, A. Saraf, C. Kim, Y.-Y. Chuang, J. Kopf, and J.-B. Huang, “Robust dynamic radiance fields,” in *Proceedings of the IEEE/CVF Conference on Computer Vision and Pattern Recognition*, 2023, pp. 13–23.
- [4] J. L. Schönberger and J.-M. Frahm, “Structure-from-motion revisited,” in *Conference on Computer Vision and Pattern Recognition (CVPR)*, 2016.
- [5] J. Wang, H. Yuan, D. Chen, Y. Zhang, X. Wang, and S. Zhang, “Modelscope text-to-video technical report,” *arXiv preprint arXiv:2308.06571*, 2023.
- [6] L. Höllein, A. Cao, A. Owens, J. Johnson, and M. Nießner, “Text2room: Extracting textured 3d meshes from 2d text-to-image models,” in *Proceedings of the IEEE/CVF International Conference on Computer Vision*, 2023, pp. 7909–7920.
- [7] L. Yang, B. Kang, Z. Huang, X. Xu, J. Feng, and H. Zhao, “Depth anything: Unleashing the power of large-scale unlabeled data,” *arXiv preprint arXiv:2401.10891*, 2024.
- [8] O. Avrahami, O. Fried, and D. Lischinski, “Blended latent diffusion,” *ACM Transactions on Graphics (TOG)*, vol. 42, no. 4, pp. 1–11, 2023.
- [9] A. Lugmayr, M. Danelljan, A. Romero, F. Yu, R. Timofte, and L. Van Gool, “Repaint: Inpainting using denoising diffusion probabilistic models,” in *Proceedings of the IEEE/CVF conference on computer vision and pattern recognition*, 2022, pp. 11 461–11 471.
- [10] Z. Yang, X. Gao, W. Zhou, S. Jiao, Y. Zhang, and X. Jin, “Deformable 3d gaussians for high-fidelity monocular dynamic scene reconstruction,” in *Proceedings of the IEEE/CVF conference on computer vision and pattern recognition*, 2024, pp. 20 331–20 341.
- [11] O. Bar-Tal, H. Chefer, O. Tov, C. Herrmann, R. Paiss, S. Zada, A. Ephrat, J. Hur, Y. Li, T. Michaeli *et al.*, “Lumiere: A space-time diffusion model for video generation,” *arXiv preprint arXiv:2401.12945*, 2024.
- [12] A. Gupta, L. Yu, K. Sohn, X. Gu, M. Hahn, L. Fei-Fei, I. Essa, L. Jiang, and J. Lezama, “Photorealistic video generation with diffusion models,” *arXiv preprint arXiv:2312.06662*, 2023.
- [13] P. Dai, F. Tan, Q. Xu, D. Futschik, R. Du, S. Fanello, X. Qi, and Y. Zhang, “Svg: 3d stereoscopic video generation via denoising frame matrix,” *arXiv preprint arXiv:2407.00367*, 2024.
- [14] J. Sohl-Dickstein, E. Weiss, N. Maheswaranathan, and S. Ganguli, “Deep unsupervised learning using nonequilibrium thermodynamics,” in *International conference on machine learning*. pmlr, 2015, pp. 2256–2265.
- [15] J. Ho, A. Jain, and P. Abbeel, “Denoising diffusion probabilistic models,” *Advances in neural information processing systems*, vol. 33, pp. 6840–6851, 2020.
- [16] W. Harvey, S. Naderiparizi, V. Masrani, C. Weilbach, and F. Wood, “Flexible diffusion modeling of long videos,” *Advances in Neural Information Processing Systems*, vol. 35, pp. 27 953–27 965, 2022.



- [17] J. Ho, W. Chan, C. Saharia, J. Whang, R. Gao, A. Gritsenko, D. P. Kingma, B. Poole, M. Norouzi, D. J. Fleet *et al.*, “Imagen video: High definition video generation with diffusion models,” *arXiv preprint arXiv:2210.02303*, 2022.
- [18] J. Ho, T. Salimans, A. Gritsenko, W. Chan, M. Norouzi, and D. J. Fleet, “Video diffusion models,” *Advances in Neural Information Processing Systems*, vol. 35, pp. 8633–8646, 2022.
- [19] U. Singer, A. Polyak, T. Hayes, X. Yin, J. An, S. Zhang, Q. Hu, H. Yang, O. Ashual, O. Gafni *et al.*, “Make-a-video: Text-to-video generation without text-video data,” *arXiv preprint arXiv:2209.14792*, 2022.
- [20] R. Rombach, A. Blattmann, D. Lorenz, P. Esser, and B. Ommer, “High-resolution image synthesis with latent diffusion models,” in *Proceedings of the IEEE/CVF conference on computer vision and pattern recognition*, 2022, pp. 10 684–10 695.
- [21] C. Saharia, W. Chan, S. Saxena, L. Li, J. Whang, E. L. Denton, K. Ghasemipour, R. Gontijo Lopes, B. Karagol Ayan, T. Salimans *et al.*, “Photorealistic text-to-image diffusion models with deep language understanding,” *Advances in neural information processing systems*, vol. 35, pp. 36 479–36 494, 2022.
- [22] A. Ramesh, P. Dhariwal, A. Nichol, C. Chu, and M. Chen, “Hierarchical text-conditional image generation with clip latents,” *arXiv preprint arXiv:2204.06125*, vol. 1, no. 2, p. 3, 2022.
- [23] Y. Guo, C. Yang, A. Rao, Y. Wang, Y. Qiao, D. Lin, and B. Dai, “Animatediff: Animate your personalized text-to-image diffusion models without specific tuning,” *arXiv preprint arXiv:2307.04725*, 2023.
- [24] A. Blattmann, R. Rombach, H. Ling, T. Dockhorn, S. W. Kim, S. Fidler, and K. Kreis, “Align your latents: High-resolution video synthesis with latent diffusion models,” in *Proceedings of the IEEE/CVF Conference on Computer Vision and Pattern Recognition*, 2023, pp. 22 563–22 575.
- [25] J. Z. Wu, Y. Ge, X. Wang, S. W. Lei, Y. Gu, Y. Shi, W. Hsu, Y. Shan, X. Qie, and M. Z. Shou, “Tune-a-video: One-shot tuning of image diffusion models for text-to-video generation,” in *Proceedings of the IEEE/CVF International Conference on Computer Vision*, 2023, pp. 7623–7633.
- [26] W. Peebles and S. Xie, “Scalable diffusion models with transformers,” in *Proceedings of the IEEE/CVF International Conference on Computer Vision*, 2023, pp. 4195–4205.
- [27] B. Mildenhall, P. P. Srinivasan, M. Tancik, J. T. Barron, R. Ramamoorthi, and R. Ng, “Nerf: Representing scenes as neural radiance fields for view synthesis,” *Communications of the ACM*, vol. 65, no. 1, pp. 99–106, 2021.
- [28] J. S. Yoon, K. Kim, O. Gallo, H. S. Park, and J. Kautz, “Novel view synthesis of dynamic scenes with globally coherent depths from a monocular camera,” in *Proceedings of the IEEE/CVF Conference on Computer Vision and Pattern Recognition*, 2020, pp. 5336–5345.
- [29] T. Li, M. Slavcheva, M. Zollhoefer, S. Green, C. Lassner, C. Kim, T. Schmidt, S. Lovegrove, M. Goesele, R. Newcombe *et al.*, “Neural 3d video synthesis from multi-view video,” in *Proceedings of the IEEE/CVF Conference on Computer Vision and Pattern Recognition*, 2022, pp. 5521–5531.
- [30] B. Kerbl, G. Kopanas, T. Leimkühler, and G. Drettakis, “3d gaussian splatting for real-time radiance field rendering,” *ACM Transactions on Graphics*, vol. 42, no. 4, pp. 1–14, 2023.
- [31] T. Müller, A. Evans, C. Schied, and A. Keller, “Instant neural graphics primitives with a multiresolution hash encoding,” *ACM transactions on graphics (TOG)*, vol. 41, no. 4, pp. 1–15, 2022.
- [32] R. Tucker and N. Snavely, “Single-view view synthesis with multiplane images,” in *Proceedings of the IEEE/CVF Conference on Computer Vision and Pattern Recognition*, 2020, pp. 551–560.
- [33] Y. Han, R. Wang, and J. Yang, “Single-view view synthesis in the wild with learned adaptive multiplane images,” in *ACM SIGGRAPH 2022 Conference Proceedings*, 2022, pp. 1–8.
- [34] X. Wang, C. Wu, S. Yin, M. Ni, J. Wang, L. Li, Z. Yang, F. Yang, L. Wang, Z. Liu *et al.*, “Learning 3d photography videos via self-supervised diffusion on single images,” *arXiv preprint arXiv:2302.10781*, 2023.
- [35] K. Park, U. Sinha, J. T. Barron, S. Bouaziz, D. B. Goldman, S. M. Seitz, and R. Martin-Brualla, “Nerfies: Deformable neural radiance fields,” in *Proceedings of the IEEE/CVF International Conference on Computer Vision*, 2021, pp. 5865–5874.
- [36] Y.-H. Huang, Y.-T. Sun, Z. Yang, X. Lyu, Y.-P. Cao, and X. Qi, “Sc-gs: Sparse-controlled gaussian splatting for editable dynamic scenes,” *arXiv preprint arXiv:2312.14937*, 2023.
- [37] K. Park, U. Sinha, P. Hedman, J. T. Barron, S. Bouaziz, D. B. Goldman, R. Martin-Brualla, and S. M. Seitz, “Hypernerf: A higher-dimensional representation for topologically varying neural radiance fields,” *arXiv preprint arXiv:2106.13228*, 2021.
- [38] Z. Li, S. Niklaus, N. Snavely, and O. Wang, “Neural scene flow fields for space-time view synthesis of dynamic scenes,” in *Proceedings of the IEEE/CVF Conference on Computer Vision and Pattern Recognition*, 2021, pp. 6498–6508.
- [39] Y.-C. Lee, Z. Zhang, K. Blackburn-Matzen, S. Niklaus, J. Zhang, J.-B. Huang, and F. Liu, “Fast view synthesis of casual videos,” *arXiv preprint arXiv:2312.02135*, 2023.
- [40] P. Dai, F. Tan, X. Yu, Y. Zhang, and X. Qi, “Go-nerf: Generating virtual objects in neural radiance fields,” *arXiv preprint arXiv:2401.05750*, 2024.
- [41] Q. Gao, Q. Xu, Z. Cao, B. Mildenhall, W. Ma, L. Chen, D. Tang, and U. Neumann, “Gaussianflow: Splatting gaussian dynamics for 4d content creation,” *arXiv preprint arXiv:2403.12365*, 2024.
- [42] H.-X. Yu, H. Duan, J. Hur, K. Sargent, M. Rubinstein, W. T. Freeman, F. Cole, D. Sun, N. Snavely, J. Wu *et al.*, “Wonderjourney: Going from anywhere to everywhere,” *arXiv preprint arXiv:2312.03884*, 2023.
- [43] Z. Chen, Y. Wang, F. Wang, Z. Wang, and H. Liu, “V3d: Video diffusion models are effective 3d generators,” *arXiv preprint arXiv:2403.06738*, 2024.
- [44] R. Liu, R. Wu, B. Van Hoorick, P. Tokmakov, S. Zakharov, and C. Vondrick, “Zero-1-to-3: Zero-shot one image to 3d object,” in *Proceedings of the IEEE/CVF International Conference on Computer Vision*, 2023, pp. 9298–9309.
- [45] L. Wang, J. R. Frisvad, M. B. Jensen, and S. A. Bigdeli, “Stereodiffusion: Training-free stereo image generation using latent diffusion models,” 2024.
- [46] Q. Zuo, X. Gu, L. Qiu, Y. Dong, Z. Zhao, W. Yuan, R. Peng, S. Zhu, Z. Dong, L. Bo *et al.*, “Videomv: Consistent multi-view generation based on large video generative model,” *arXiv preprint arXiv:2403.12010*, 2024.
- [47] M.-L. Shih, S.-Y. Su, J. Kopf, and J.-B. Huang, “3d photography using context-aware layered depth inpainting,” in *Proceedings of the IEEE/CVF Conference on Computer Vision and Pattern Recognition*, 2020, pp. 8028–8038.
- [48] V. Jampani, H. Chang, K. Sargent, A. Kar, R. Tucker, M. Krainin, D. Kaeser, W. T. Freeman, D. Salesin, B. Curless *et al.*, “Slide: Single image 3d photography with soft layering and depth-aware inpainting,” in *Proceedings of the IEEE/CVF International Conference on Computer Vision*, 2021, pp. 12 518–12 527.
- [49] S. Zhou, C. Li, K. C. Chan, and C. C. Loy, “Propainter: Improving propagation and transformer for video inpainting,” in *Proceedings of the IEEE/CVF International Conference on Computer Vision*, 2023, pp. 10 477–10 486.
- [50] Z. Li, C.-Z. Lu, J. Qin, C.-L. Guo, and M.-M. Cheng, “Towards an end-to-end framework for flow-guided video inpainting,” in *Proceedings of the IEEE/CVF conference on computer vision and pattern recognition*, 2022, pp. 17 562–17 571.
- [51] J. Xie, R. Girshick, and A. Farhadi, “Deep3d: Fully automatic 2d-to-3d video conversion with deep convolutional neural networks,” in *Computer Vision—ECCV 2016: 14th European Conference, Amsterdam, The Netherlands, October 11–14, 2016, Proceedings, Part IV 14*. Springer, 2016, pp. 842–857.
- [52] A. Karnewar, A. Vedaldi, D. Novotny, and N. J. Mitra, “Holodiffusion: Training a 3d diffusion model using 2d images,” in *Proceedings of the IEEE/CVF conference on computer vision and pattern recognition*, 2023, pp. 18 423–18 433.
- [53] Z. Teed and J. Deng, “Raft: Recurrent all-pairs field transforms for optical flow,” in *Computer Vision—ECCV 2020: 16th European Conference, Glasgow, UK, August 23–28, 2020, Proceedings, Part II 16*. Springer, 2020, pp. 402–419.
- [54] P. Dai, Y. Zhang, Z. Li, S. Liu, and B. Zeng, “Neural point cloud rendering via multi-plane projection,” in *Proceedings of the IEEE/CVF Conference on Computer Vision and Pattern Recognition*, 2020, pp. 7830–7839.
- [55] T. Zhou, R. Tucker, J. Flynn, G. Fyffe, and N. Snavely, “Stereo magnification: Learning view synthesis using multiplane images,” *arXiv preprint arXiv:1805.09817*, 2018.
- [56] P. Pérez, M. Gangnet, and A. Blake, “Poisson image editing,” in *Seminal Graphics Papers: Pushing the Boundaries, Volume 2*, 2023, pp. 577–582.
- [57] C. Rota, M. Buzzelli, and J. van de Weijer, “Enhancing perceptual quality in video super-resolution through temporally-consistent detail synthesis using diffusion models,” in *European Conference on Computer Vision*. Springer, 2024, pp. 36–53.
- [58] T. Liu, Z. Huang, Z. Chen, G. Wang, S. Hu, L. Shen, H. Sun, Z. Cao, W. Li, and Z. Liu, “Free4d: Tuning-free 4d scene generation with spatial-temporal consistency,” *arXiv preprint arXiv:2503.20785*, 2025.

- [59] J. Zhang, C. Herrmann, J. Hur, V. Jampani, T. Darrell, F. Cole, D. Sun, and M.-H. Yang, “Monst3r: A simple approach for estimating geometry in the presence of motion,” *arXiv preprint arXiv:2410.03825*, 2024.
- [60] Z. Li, X. Liu, N. Drenkow, A. Ding, F. X. Creighton, R. H. Taylor, and M. Unberath, “Revisiting stereo depth estimation from a sequence-to-sequence perspective with transformers,” in *Proceedings of the IEEE/CVF International Conference on Computer Vision (ICCV)*, October 2021, pp. 6197–6206.
- [61] J. Hessel, A. Holtzman, M. Forbes, R. L. Bras, and Y. Choi, “CLIPScore: a reference-free evaluation metric for image captioning,” in *EMNLP*, 2021.
- [62] C. Schuhmann, R. Beaumont, R. Vencu, C. Gordon, R. Wightman, M. Cherti, T. Coombes, A. Katta, C. Mullis, M. Wortsman *et al.*, “Laion-5b: An open large-scale dataset for training next generation image-text models,” *Advances in Neural Information Processing Systems*, vol. 35, pp. 25 278–25 294, 2022.
- [63] H. Wu, E. Zhang, L. Liao, C. Chen, J. Hou, A. Wang, W. Sun, Q. Yan, and W. Lin, “Exploring video quality assessment on user generated contents from aesthetic and technical perspectives,” in *Proceedings of the IEEE/CVF International Conference on Computer Vision*, 2023, pp. 20 144–20 154.
- [64] T. Unterthiner, S. van Steenkiste, K. Kurach, R. Marinier, M. Michalski, and S. Gelly, “Fvd: A new metric for video generation,” 2019.
- [65] R. Likert, “A Technique for the Measurement of Attitudes,” *Archives of Psychology*, 1932.
- [66] A. Radford, J. W. Kim, C. Hallacy, A. Ramesh, G. Goh, S. Agarwal, G. Sastry, A. Askell, P. Mishkin, J. Clark *et al.*, “Learning transferable visual models from natural language supervision,” in *International conference on machine learning*. PMLR, 2021, pp. 8748–8763.
- [67] S. Zhengwentai, “clip-score: CLIP Score for PyTorch,” <https://github.com/taited/clip-score>, March 2023, version 0.1.1.